



**UHASSELT**



**Maastricht University**

KNOWLEDGE IN ACTION

## **Faculty of Medicine and Life Sciences** **School for Life Sciences**

Master of Biomedical Sciences

### **Master's thesis**

***A first step towards the development of a droplet-based microfluidic device for the production of artificial membranes***

#### **Steff Borgmans**

Thesis presented in fulfillment of the requirements for the degree of Master of Biomedical Sciences, specialization Bioelectronics and Nanotechnology

#### **SUPERVISOR :**

Prof. dr. ir. Ronald THOELEN

#### **MENTOR :**

De heer Stijn DILISSEN

Transnational University Limburg is a unique collaboration of two universities in two countries: the University of Hasselt and Maastricht University.



**UHASSELT**

KNOWLEDGE IN ACTION

[www.uhasselt.be](http://www.uhasselt.be)  
Universiteit Hasselt  
Campus Hasselt:  
Martelarenlaan 42 | 3500 Hasselt  
Campus Diepenbeek:  
Agoralaan Gebouw D | 3590 Diepenbeek

**2021**  
**2022**



**UHASSELT**

KNOWLEDGE IN ACTION



**Maastricht University**

# **Faculty of Medicine and Life Sciences**

## ***School for Life Sciences***

Master of Biomedical Sciences

### ***Master's thesis***

***A first step towards the development of a droplet-based microfluidic device for the production of artificial membranes***

#### **Steff Borgmans**

Thesis presented in fulfillment of the requirements for the degree of Master of Biomedical Sciences, specialization Bioelectronics and Nanotechnology

#### **SUPERVISOR :**

Prof. dr. ir. Ronald THOELEN

#### **MENTOR :**

De heer Stijn DILISSEN



**A first step towards the development of a droplet-based microfluidic device for the production of artificial membranes**Steff Borgmans<sup>1,2,3</sup>, Stijn Dilissen<sup>1,2,3</sup>, Jelle Hendrix<sup>3</sup> and Ronald Thoelen<sup>1,2</sup><sup>1</sup>Institute for Materials Research IMO, Hasselt University, Wetenschapspark 1, B-3590 Diepenbeek, Belgium<sup>2</sup>IMOMEC Division, IMEC vzw, Wetenschapspark 1, B-3590 Diepenbeek, Belgium<sup>3</sup>Dynamic Bioimaging Lab, Advanced Optical Microscopy Centre and Biomedical Research Institute, Hasselt University, Agoralaan C (BIOMED) - B-3590 Diepenbeek, Belgium\*Running title: *A microfluidic chip for giant liposome synthesis*

To whom correspondence should be addressed: Ronald Thoelen, Tel: +32 (11) 26 88 26; Email: Ronald.thoelen@uhasselt.be

**Keywords:** Droplet microfluidics, Numerical modeling, Artificial membranes, Photo Lithography, Water-in-oil droplets**ABSTRACT**

Lipid-based vesicles and giant unilamellar vesicles (GUVs), have repeatedly shown their potential as versatile tools in the life sciences. They have been widely used as model systems, which mimic certain aspects of living cells, to better understand membrane-bound processes. Additionally, they can serve as carrier systems for drug delivery applications. Conventional GUV synthesis methods offer a low level of control and result in polydisperse products. Although, a shift to microfluidics enabled the high-throughput production of monodisperse vesicles with high encapsulation efficiencies, their post-production manipulability has remained limited to date. The assembly of droplet-stabilized GUVs (dsGUVs), which offer greater stability, is therefore necessary to both incorporate specific components in these artificial membranes and improve the tunability of the model system. In this work, we demonstrate a first step towards the development of a droplet-based microfluidic device. Numerical simulations were utilized to validate the design of the circuit. The optimal in-house fabrication procedures were determined and the resulting devices were utilized for both *in silico* and *in vitro* investigations. Both the resulting droplet size and generation frequency were increased by increasing the aqueous flow

rate. Increasing the continuous phase flow rate, resulted in smaller droplets and a greater generation frequency. Lastly, devices with broader channels produced bigger droplets at a slower rate as compared to narrow channels. The formation of water-in-oil droplets serves as a foundation for the assembly of dsGUVs in the following stages of this project and the further development of droplet-based microfluidic devices for synthetic biology applications and beyond.

**INTRODUCTION**

Lipid-based vesicles could offer great functionality for various applications in the life sciences (1). Firstly, implementing these vesicles as carrier systems for drug delivery purposes has seen significant advances in recent years (1-3). Here, lipid vesicles have been utilized as vehicles for targeted intracellular cargo delivery (1). Another example of their potential as carrier systems is found in the field of nanomedicine, which uses nanotechnology to diagnose or treat different diseases (3). The use of lipid-based vesicles as carrier systems is not exclusively limited to drug delivery applications. They can also be useful to manipulate cell-to-cell signaling. For example, the promotion of wound healing and neovascularization therapy, which has also been

demonstrated using synthetic extracellular vesicles (2). Secondly, they allow for the construction of membrane-bound artificial cells. This diverse class of lipid-based synthetic cells offers a platform for prospective applications such as programmable microreactors and *in vivo* diagnostics (4). Moreover, they can be utilized as biomimetic structures to investigate specific aspects of living cells providing valuable insights into different membrane-based processes (1, 5). These vesicles can be engineered to perform specific functions without wasting energy and resources on auxiliary functions. Thus, this reduced complexity makes it easier to study them and to maintain control over variables (5). This application can be specifically useful to perform drug screening for G-protein-coupled receptors (GPCRs). It is often necessary to reconstitute GPCRs in its physiological environment since purified GPCRs offer low stability, which makes the screening process challenging (6). About 30 – 40% of clinically approved drugs target GPCR signaling pathways and they play a role in an incredible array of functions in the human body (6, 7). Gaining a better understanding of the interaction between certain drugs and membrane receptors such as GPCRs would therefore greatly improve further developments in modern medicine (7).

Lipid-based vehicles can be split into three types based on their size: small, large or giant unilamellar vesicles (SUVs, LUVs or GUVs) (8). With diameters around ~100 nm, SUVs are often utilized as carriers for targeted drug therapy in the pharmaceutical industry. This type of vesicle is also suited as a platform for the reconstitution of membrane proteins such as bo<sub>3</sub> oxidase and ATP synthase (9). Additionally, they have served as delivery systems in the cosmetic and food industries (1). While SUVs have certain benefits for this delivery application, their small dimensions limit the amount of active compounds that can be loaded (1).

In contrast to their smaller counterparts, giant unilamellar vesicles (GUVs), with diameters exceeding 1 μm, offer the possibility to entrap larger structures or higher quantities of active compounds as carrier system (1, 3). Moreover, the greater storage capacity of GUVs can be utilized to modify the cell-carrier interaction by incorporating

stimulus-responsive ligands in addition to the drugs (3). These stimulus-responsive ligands are tailored to the environment of the drug delivery target, which allows for improved internalization or fusogenic properties (3).

Micron-scale compartments, enclosed by a phospholipid bilayer, are also ideal model systems to mimic certain aspects of living cells (10). This way, specific membrane-based processes, such as calcium regulation (11) or the different functions of GPCRs (6), can be investigated in less complex and more practical environments. The most frequently chosen model system in synthetic biology are GUVs (12, 13). They are composed of lipid membranes, and match the dimensions of eukaryotic cells (12). Furthermore, the similarity to the natural cell membrane allows the incorporation of cellular constituents while retaining their functionality (13).

The production process of synthetic lipid-based vesicles can be divided into two general strategies (5). First, in the top-down approach vesicles or cells are obtained from natural sources, and transformed into a modified product (5). However, these natural structures consist of complex components, and their acquisition often requires extensive and error-prone procedures (2). The second approach, the bottom-up method, builds up biomimetic structures from scratch using simple chemical or biological elements (5). In the context of bottom-up synthetic biology, current research focuses on the fabrication of artificial cells and synthetic cellular components (1). Such structures have been constructed using a variety of amphiphilic vesicle forming molecules, including lipid-based water-in-oil droplets (8, 13).

The synthesis of GUVs is often achieved by electro-formation (14), gentle hydration (15) and solvent evaporation (16). However, all the aforementioned techniques create polydisperse products and have a low encapsulation efficiency for cargo loading. The flexibility of these methods is also limited since they often require specific buffers and lipid compositions (13). Additional challenges in utilizing lipid-based vesicles consist of the sensitivity of phospholipids to both pH changes and high ionic strength conditions which

cause chemical and mechanical instabilities (17-19).

Recently, microfluidic technologies have become increasingly implemented in bottom-up synthetic biology (3, 20). Microfluidic systems involve the manipulation of fluids in channels with micrometer dimensions (1–1000  $\mu\text{m}$ ) (5). As illustrated by the Reynolds number ( $Re_D$ ), the fluid dynamics are mainly dependent on the fluid density ( $\rho$ ), flow rate ( $v$ ), hydraulic diameter ( $D_h$ ) and viscosity ( $\mu$ ):

$$Re_D = \frac{\rho * v * D_h}{\mu}$$

Accordingly, the viscous forces will dominate the inertial forces when the fluids are confined in these micron-sized regions. A laminar flow is therefore expected over a turbulent flow in microfluidic systems since their channel dimensions are very small. A laminar flow is seen at a low Reynolds number ( $Re_D < 2300$ ) (5).

This shift to microfluidics enabled the development of improved GUV production techniques such as water-in-oil-in-water (W/O/W) double-emulsion methods (21) and water-in-oil (W/O) single-emulsion droplets (22). This way, the high-throughput production of monodisperse vesicles with a high encapsulation efficiency was achieved (10). However, the resulting GUVs remain mechanically and chemically unstable after formation, limiting their post-production manipulability (13).

A solution to this problem was demonstrated by Weiss *et al.* with the assembly of copolymer-stabilized water-in-oil compartments (8). This construct consists of a spherical lipid bilayer inside a water-in-oil droplet, which in turn is stabilized by a custom-synthesized block-copolymer surfactant (23). These droplet-stabilized GUVs (dsGUVs) can be manipulated at high throughput using microfluidic technology since their stability is maintained by the continuous oil phase and the oil additives (8, 24). Further research in this field illustrated the high level of tunability during the charge-mediated assembly of GUVs. Thus, both single- and multicompartment dsGUVs could be generated by altering the ratio between charged and uncharged fluorosurfactants (23). The ability to

generate GUVs with various lipid compositions allows the fine-tuning of physicochemical properties such as surface charge, fluidity, and stiffness (3). As noted, one of the most interesting properties of dsGUVs is the option to manipulate them after formation with pico-injection technology (8). By switching an electric field on and off, we can selectively inject drops, at kilohertz rates. This way, precise amounts of different molecules and proteins can be sequentially loaded into the more mechanically and chemically stable compartments (8). Moreover, the charge-mediated assembly of dsGUVs permits the reconstitution of transmembrane proteins into the lipid bilayer to study specific membrane-based processes (3). Afterwards, these functionalized GUVs can be released from the stabilizing droplets into water for further investigations in physiologically relevant environments (8).

In this work, we demonstrate a first step towards the development of a droplet-based microfluidic device for the production of artificial membranes in the form of dsGUVs. The proposed microfluidic device directs two fluid phases towards a flow-focusing junction in order to generate water-in-oil droplets. Here, the oil is the continuous phase, supporting the dispersed or aqueous phase. Using microfluidics allows a high-throughput generation of monodisperse droplets, together with considerable control over the particle size, and great stability (20, 23). The in-house fabrication of microfluidic devices is an expensive and time-consuming process. Thus, the initial design of this device was investigated *in silico* in the COMSOL Multiphysics software. In a second step, we determined the optimal in-house fabrication procedures to produce the actual devices. Next, the resulting microfluidic devices were investigated *in vitro* by characterizing their droplet-formation capabilities. Finally, we compared the experimental results and the numerical simulations to improve the development process of future devices.

## EXPERIMENTAL PROCEDURES

*Materials* – Hellmanex (Hellma), SU-8 3000 series photoresist (Kayaku, MicroChem), SU-8 2000 thinner (Kayaku, MicroChem), SU-8 developer (Kayaku, MicroChem), Omnicat

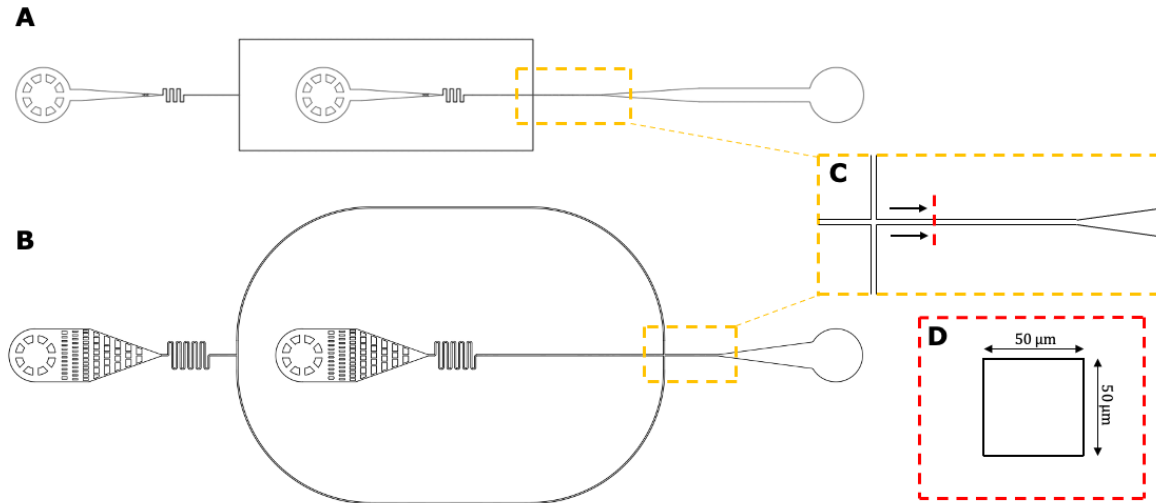


**Fig. 1 – Schematic overview of the microfluidic circuits.** (A) Initial design of the device. Length = 60 mm. Three versions with channel widths of 200, 100 and 50 μm were obtained. (B) Final design of the device with the addition of a filtering module at each inlet. Length = 30 mm. Two versions of this circuit with channel widths of 50 and 30 μm were created. (C) The flow-focusing junction of both devices. (D) A cross-sectional view of the channel, which has a height and a width of 50 μm.

(Kayaku, MicroChem), polydimethylsiloxane (PDMS) elastomer base (Sylgrad 184), PDMS curing agent (Sylgrad 184), HFE-7500 fluorinated oil (3M, Novec), and high-performance surfactant dSurf (Fluigent).

*Microfluidic Circuit Design* – The schematics of the microfluidic circuits were drawn in AutoCAD 2022. The initial structure was based on related microfluidic devices, which were utilized for similar applications. The design was further modified based on the attained data from the numerical simulations. In **Fig. 1**, the schematic view of both the initial model (A) and final model (B) are shown.

*Numerical Simulations* – The COMSOL Multiphysics 5.3 software was employed to perform the numerical analysis of the droplet microfluidic circuit. In order to reduce the complexity of the simulations, only the most vital section of the circuit, namely the flow-focusing junction as shown in **Fig. 1(C, D)**, is modelled and constructed in COMSOL in 2D to save computational power and time. The model consists of a two-phase fluid flow and a level set model with incompressible, Newtonian fluids and low Reynolds numbers (laminar flow). The Phase field

method was applied to solve this model in a time-dependent manner. This method constantly determined the fluid-fluid diffuse interface while maintaining the complete system at its lowest possible total energy. This resulted in a model, which is generally defined by momentum conservation equations (Navier-Stokes) and a continuity equation for incompressible phases:

$$\rho \frac{\partial U}{\partial t} + \rho(U \cdot \nabla)U = \nabla \cdot [-pI + \mu(\nabla U + (\nabla U)^T)] - 12 \frac{\mu U}{d_z^2} + F$$

$$\rho(\nabla \cdot U) = 0$$

where  $t$  is time (s),  $p$  is pressure (Pa),  $U$  is velocity vector (m/s),  $F$  is volume forces ( $N/m^3$ ) and  $d_z$  is channel thickness (m). The dynamic viscosity  $\mu$  (Pa.s) and fluid density  $\rho$  ( $kg/m^3$ ) are based on the viscosity and density of dispersed- and continuous phases. The COMSOL material library was utilized to define the material of the channel boundaries as polydimethylsiloxane (PDMS). Similarly, this library was used to define the dispersed phase and continuous phase for both water and transformer oil, respectively. The initial fluid velocity was zero in the whole circuit, and the pressure at the outlet was assumed to be equal to the atmospheric pressure. Additionally, the wetted wall boundary condition was set with a contact angle of

135° given the hydrophobic nature of PDMS. At the inlets, two different conditions were applied as inputs for velocity. The velocity condition was used to set a constant inflow velocity (m/s), and the laminar inflow condition was utilized to define a constant flow rate (m<sup>3</sup>/s) and the entrance length (m) of the inlets. Lastly, the effective droplet diameter ( $d_{eff}$ ) was automatically calculated by the following equation:

$$d_{eff} = 2 * \sqrt{\left(\frac{\text{intop1}((\text{phils} > 0.5) * (x > 750[\mu\text{m}])))}{\pi i}\right)}$$

where intop1 is an integration function, phils ( $\phi$ ) is a dimensionless number that characterizes the volume fraction of both phases, and  $x$  defines the measurement position in the microchannel.

**Mask Fabrication** – A chrome mask of the designed microfluidic circuits, which was fabricated using a laser beam pattern generator, was ordered from Delta Mask b.v., Netherlands. The mask design was drawn in AutoCAD 2022.

**Master Preparation** – A glass cover slide (26 \* 76 \* 1 mm, Thermo Scientific) or a silicon wafer (diameter of 127 mm) was selected to serve as a foundation for the master. First, a thorough cleaning procedure was performed in an ultrasonic cleaning bath (Fisher Scientific, S series) by sequentially placing the substrate in the following solutions for a given duration: 30 min in 2 % Hellmanex – MilliQ solution, 20 min in MilliQ, 10 min in Acetone, and 10 min in Isopropyl alcohol. Afterwards, the substrate was placed in the spin-coating system (POLOS spin150i, PoliFab). For glass slides, a thin layer of Omnicoat was spin-coated on top and the slide was baked on a hot plate (Stuart Digital, Fisher Scientific) at 200 °C for 1 min to improve the adhesion between a glass slide and the photoresist. A 50- $\mu\text{m}$ -thick layer of the negative photoresist SU-8 3000 series was spin-

coated directly on top of the substrate, according to **Table 1**. Next, the substrate was soft baked on a hot plate (Stuart Digital, Fisher Scientific) at 95 °C for 15 to 30 minutes. Afterwards, the substrates were wrapped in aluminum foil and stored in a dark location.

**Master Fabrication** – The substrate was placed under the illumination device (Karl Suss Mask Aligner) and the mask was manually positioned on top of the substrate. Two pieces of transparent tape were placed on either side of the master to function as a spacer with a height of 50  $\mu\text{m}$ . After correctly aligning both components, the device was activated and the photoresist was exposed to UV radiation (380 nm) for one minute. Next, a post exposure bake (PEB) was performed on a hot plate at 95°C for 5 minutes. The substrate was then placed in a SU-8 developer solution for 12 to 15 minutes and washed with isopropyl alcohol (IPA) to remove the unexposed photoresist from the substrate.

**Replica Fabrication** – A 10:1 PDMS elastomer base: curing agent mixture was prepared and placed in a vacuum chamber for 1h to remove any air bubbles. This mixture was poured onto the master wafer to create a PDMS-based replica. It was placed back into a vacuum chamber for 30 minutes and then into an oven to cure the replica at 50°C overnight. After the curing process, the replica was cut out of the bulk material and the passages to the two inlets and the outlet were created using a biopsy punch (1 mm diameter, Miltex). Next, a thin microscope slide (24 \* 50 \* 0.13-0.16 mm, Thermo Scientific) and the PDMS replica were treated with UV ozone (PSD series, Digital UV Ozone System, Novascan) for 15 minutes and manually bonded together. The bonded device was finished by a heat treatment at 80°C for 1h.

**Table 1** – Spin-coat settings to form a photoresist SU-8 3000 series layer of 50  $\mu\text{m}$ .

Photoresist	Step 1			Step 2		
	Velocity (rpm)	Acceleration (rpm/s)	Duration (s)	Velocity (rpm)	Acceleration (rpm/s)	Duration (s)
SU-8 3050	500	100	10	3000	300	30
SU-8 3035	500	100	10	2000	300	30
SU-8 3025	500	100	10	1400	300	30

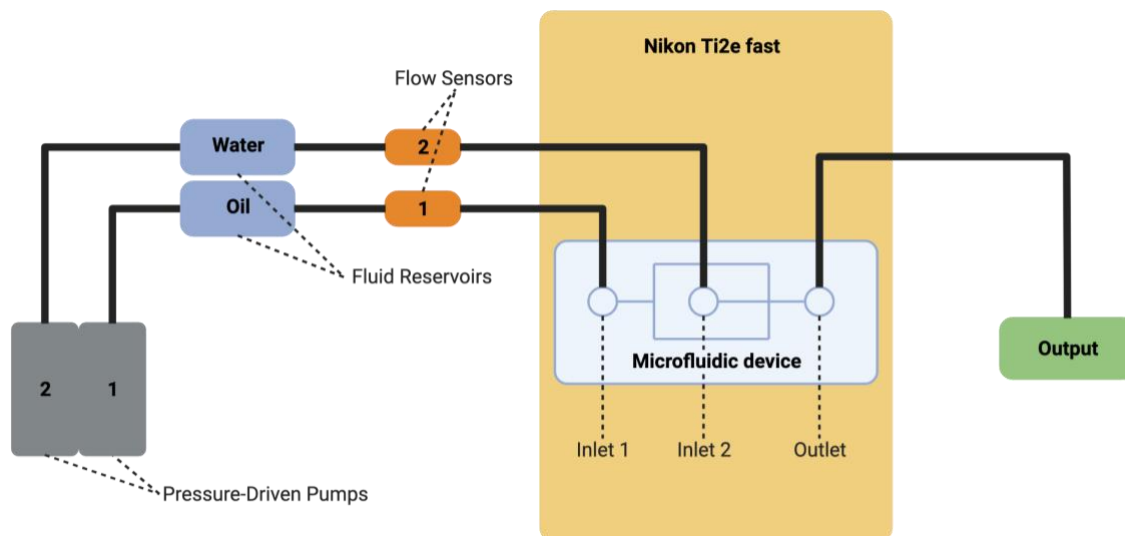


**Fig. 2 – A visual representation of the experimental setup.** Two pressure-driven pumps were utilized to control the inflow condition of both an oil and a water flow. Two corresponding flow sensors were inserted in the setup when mentioned. The microfluidic device was positioned in a Nikon Ti2e fast large FOV, widefield microscope. The pressure at the outlet was equal to the atmospheric pressure.

*Device characterization* – The general appearance and the achieved resolution of both the master and the PDMS replica were assessed using light microscopy (Zeiss, Axio Vert.A1 FL, inverted microscope). The channel width of the devices was obtained from these images in ImageJ. A Dektak XT profilometer (Bruker) was utilized to determine the channel heights. Lastly, the fluid flow patterns inside the microchannels were investigated using a microprocessor controlled dispensing pump (Ismatec, IPC) and a contrast fluid, namely methyl blue.

*Experimental setup* – The experimental measurements were performed on a Nikon Ti2e fast, large FOV widefield microscope. The recordings were performed in bright field mode using a 4x objective lens. The general setup included two pressure-driven pumps (Fluigent FlowEZ, UNEUP) and corresponding flow sensors (Fluigent) as shown in **Fig. 2**. According to this figure, the first pump was attached to the fluid reservoir of the continuous phase, and the second pump was connected to the dispersed phase reservoir. Each reservoir was further connected to their corresponding inlet of the device after passing through a flow sensor. The continuous phase consisted of HFE-7500 fluorinated oil and 2% of a

high-performance surfactant dSurf. Deionized water was utilized as the dispersed phase. The microchannels were contained in a horizontal plane to avoid most gravitational effects. The pumps were operated in a flow-driven mode or a pressure-driven mode.

*Data analysis* – The resulting data of the experimental measurements was analyzed in ImageJ, Fiji. Both the droplet generation frequency  $f$  and the droplet diameters were assessed for each measurement manually. The following symbol:  $\pm$  illustrates the standard deviation.

## RESULTS AND DISCUSSION

*Initial Numerical Investigation* – The development of a droplet-based microfluidic device started by performing simulations of several prototype circuits. The resulting device should be able to produce water-in-oil droplets at the flow-focusing junction. Moreover, the droplet size should be both consistent and in a 1 to 1000  $\mu\text{m}$  range to serve as stabilizing compartments for dsGUVs. An initial design of the microfluidic device was determined, as shown in **Fig. 1(A)**, based on the acquired numerical data. Further *in silico* investigations demonstrated the influence of both the circuit geometry and the flow velocities on

the resulting droplet sizes. Ratio  $Q_d/Q_c$  defines the ratio of the inflow boundary condition of the dispersed phase ( $Q_d$ ) to the inflow boundary condition of the continuous phase ( $Q_c$ ).

In a virtual 50- $\mu\text{m}$ -wide channel, the droplet size could be manipulated by adjusting the velocity of the oil phase at a constant aqueous velocity of 0.009 m/s. In this case, the channel height was unspecified and virtually infinite in the 2D simulations of Fig. 3(A, B, D, E). According to Fig. 3(A, B), the droplet diameters can be controlled in a range from approximately 75  $\mu\text{m}$  to 40  $\mu\text{m}$  by increasing the oil velocity from 0.01 to 0.09 m/s. Similarly, the droplet diameter could be altered from 125  $\mu\text{m}$  to 95  $\mu\text{m}$  in a 100- $\mu\text{m}$ -wide channel by increasing the oil velocity from 0.01 to 0.04 m/s at a constant aqueous flow velocity of 0.009 m/s. From Fig. 3(B) it is obvious that the droplet diameter increases as the ratio  $Q_d/Q_c$  decreases. Furthermore, the droplet size is greatly defined by the geometry of the circuit. In Fig. 3(A, B), the

effect of different channel widths on the droplet diameter can also be seen. Here, the droplet sizes are greater in a 100- $\mu\text{m}$ -wide channel than a 50- $\mu\text{m}$ -wide channel at similar flow velocities. In Fig. 3(D, E), it is further demonstrated that both the flow velocities and the channel width have an effect on the droplet generation frequency  $f$ . The number of droplets per second increases as the oil velocity is increased at a constant aqueous velocity. Additionally, a narrow channel will generate droplets at a higher frequency than a wider channel at the same flow velocities. The same flow volume passes through both channels, but the droplet frequency differs. In a narrow channel, each generated droplet is smaller in size, and thus a smaller fraction of the flow volume is consumed per droplet. This way, less droplets are generated in a 100- $\mu\text{m}$ -wide channel since each droplet utilizes a higher fraction of the same flow volume. As seen in Fig. 3(E), a decreasing droplet generation frequency as the difference between  $Q_d$  and  $Q_c$

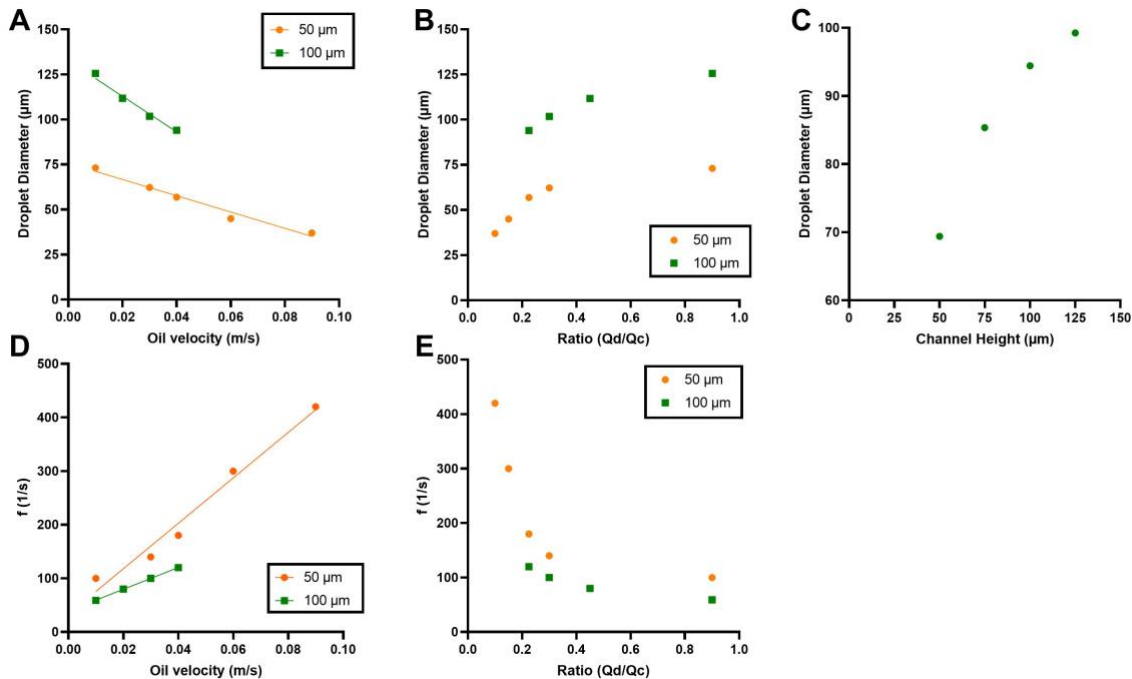


**Fig. 3 – Initial numerical investigation of the droplet tunability.** (A, B, D, E) Constant aqueous velocity = 0.009 m/s. (A, B, D, E) The channel height is either 50  $\mu\text{m}$  or 100  $\mu\text{m}$ , which is illustrated in orange or green, respectively. (A) The effect of an increasing oil velocity on the droplet size. (B) The resulting droplet diameter in reaction to the ratio  $Q_d/Q_c$ . (C) Influence of different channel heights on the droplet size. Channel width is 100 microns, Oil flow rate is 2000  $\mu\text{L/h}$  and Aqueous flow rate is 200  $\mu\text{L/h}$ . (D) The effect of an increasing oil inflow velocity on the droplet generation frequency  $f$ . (E) The resulting droplet diameter over the changing ratio of  $Q_d$  to  $Q_c$ .

decreases. Altering the channel height at constant flow velocities also influences the resulting droplet sizes, as shown in Fig. 3(C). Thus, the droplet size decreased as the channel height was lowered at constant inflow conditions for both phases.

Finally, three versions of this design with channel widths of 50, 100, and 200 microns were proposed for two main reasons. Firstly, it was still unclear how accurate the in-house lithography equipment was. Secondly, the effect of different channel geometries could be investigated *in vitro* in this manner. This would allow the user to obtain better control over the resulting droplet size by utilizing either broader or narrower channels for specific applications. After these initial simulations, we tried to transform the chosen circuit designs into actual devices to carry out *in vitro* investigations.

*Photo- and Soft Lithography* – The complete development process of the microfluidic devices is illustrated in Fig. 4. To ensure good attachment of the SU-8 3035 photoresist to the cover slip, two approaches were explored. First, three different glass surface treatments to improve the photoresist-glass adhesion were evaluated. Both a heat and an UV-ozone -treatment were proven ineffective since the master still loosened afterwards. Nonetheless,

the adhesion of the master on glass slides was improved by spin-coating a thin layer of Omnicoat before applying the photoresist. The second approach included the removal of any vulnerable elements, such as acute corners, from the microfluidic circuit design. Further modifications to the design were the addition of a filtering module after each inlet. This prevents the presence of contaminations in the most vital parts of the microfluidic circuit. These contaminations can be dust particles or residues of PDMS. Additionally, the length of the whole circuit was reduced from 60 mm to 30 mm. This would allow us to use a smaller substrate holder since the original substrate holder was not functioning correctly at the time. The improved circuit design was realized in two variants with channel widths of 30 and 50 microns.

A second complication was found when operating the illumination device since the mask had to be manually aligned above the photoresist, and this device only operated in contact mode. Thus, to reduce the stickiness of the photoresist, the soft bake time was increased from 15 minutes to 30 minutes and a spacer was utilized. The implementation of a spacer seemed to slightly reduce the achieved resolution of the master, as illustrated in Supplementary Fig. 1. However, only two masters were successfully fabricated

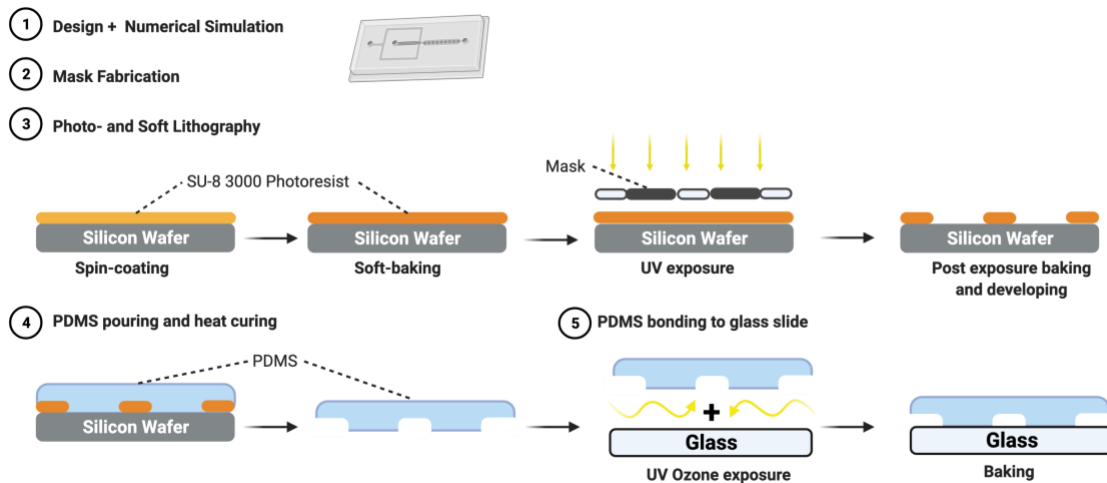


**Fig. 4 – The development process of the proposed droplet-based microfluidic device.** 1) The chip design was based on 2D numerical simulations of the flow-focusing junction. 2) The microfluidic pattern was transferred on a chrome mask using a laser beam generator. 3) Photo- and soft lithography techniques were applied to fabricate a master of the device on a silicon wafer. 4) A PDMS-based replica was made from the corresponding master. 5) The device was finished by bonding the PDMS replica on a glass cover slide.

without the use of a spacer. These measurements should be repeated on additional masters to verify this observation. The utilization of a more sophisticated illumination device, which can operate in proximity mode, could potentially also prevent these complications. Lastly, the SU-8 3035 photoresist, which has a viscosity of 7400 cSt, was replaced by the SU-8 3025 photoresist, which has a lower viscosity of 4400 cSt. This slightly reduced the presence of air inside the photoresist when it is applied on the glass slide, and a height of 50 microns was still achievable using this more manageable dilution.

*Master - and Replica Characterization* – The resulting masters were characterized after production to further evaluate their quality and to adjust the synthesis process if necessary. Next, a PDMS-based replica was made and both the master and replica were characterized in a similar manner. Light microscopy was utilized to assess the state of the photoresist and PDMS, and to determine the achieved resolution. When a microfluidic circuit with a channel width of 50  $\mu\text{m}$  was developed, the resulting master channel widths ranged from 51 to 58  $\mu\text{m}$  for the different masters. On average, this

channel width was 54.3  $\mu\text{m}$  over fifteen individual masters. However, the channel width was more consistent within the same master. There was no noticeable difference in channel width between the masters and their related replicas, as shown in **Supplementary Fig. S2**.

The height of the resulting masters, which were synthesized using the SU-8 3025 dilution, was measured with a profilometer. The heights varied between each master and ranged from 42 to 72  $\mu\text{m}$ . The average height of the masters was found to be 58.58  $\mu\text{m}$  over 12 measurements. For masters, which were synthesized using SU-8 3035, the average height was 73.3  $\mu\text{m}$ . However, only three measurements were performed this dilution of the photoresist. The PDMS-based replicas were not compatible with the profilometer since this material lacks rigidity and deforms during the measurements.

A detailed visualization of two finished devices, which consist of the PDMS-based replicas bonded on a glass slide, is demonstrated in **Fig. 5**. Both devices were created using the mask of the improved microfluidic circuit (see **Fig. 1(B)**). Moreover, the masters were synthesized on top of a silicon wafer instead of a glass slide. The resulting

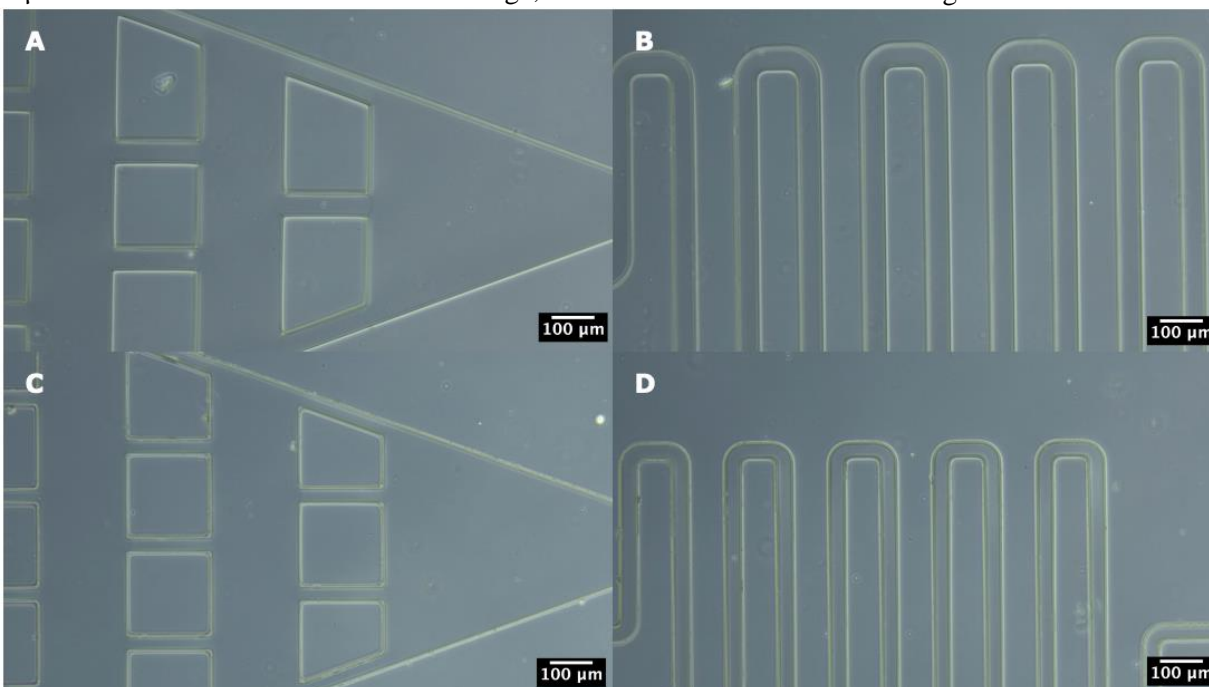


**Fig. 5** – Two finished devices: PDMS-based replicas bonded on a glass slide. (A, B) Device with channel width of 50  $\mu\text{m}$ . (C, D) Device with channel width of 30  $\mu\text{m}$ . (A, C) The filter module at the inlet. (B, D) The S-curves after the filtering module.

masters were more robust due to the strong adhesion between the photoresist and the silicon. In **Fig. 5(A, B)**, two regions of a device with 50- $\mu\text{m}$ -wide channels can be seen. The average channel width of nine similar finished devices was  $51.93 \pm 1.44 \mu\text{m}$ . Next, the two corresponding regions of a device with 30- $\mu\text{m}$ -wide channels was illustrated in **Fig. 5(C, D)**. In this case, seven similar devices were evaluated and the average channel width was  $32.69 \pm 0.83 \mu\text{m}$ . Afterwards, we started a new *in silico* investigation since the dimensions of the microfluidic device were altered during the previous improvements of the circuit.

*Numerical Investigation* – Following the design of the improved circuit in **Fig. 1(B)**, a more detailed *in silico* investigation was performed on a similar flow-focusing junction. This virtual junction has both a channel width and height of 50  $\mu\text{m}$ . As noted in **Fig. 3**, the droplet size could be altered by adjusting the velocity of the oil phase at a constant aqueous velocity. However, it would be

difficult to define the velocities of the two fluid phases during an *in vitro* investigation. Thus, the laminar inflow condition of the two fluids was changed to a given flow rate in  $\mu\text{L/h}$ . This way, it would be more manageable to compare this data to the experimental investigation. At a constant aqueous flow rate of 100  $\mu\text{L/h}$ , the oil flow rate was increased from 400 to 1000  $\mu\text{L/h}$ . By increasing the oil flow rate, the resulting droplet diameters were reduced from 54 to 39  $\mu\text{m}$  in **Fig. 6(A)**. Moreover, the droplet generation frequency became greater as this rate was increased, as shown in **Fig. 6(D)**. A similar investigation was performed on the influence of the aqueous flow rate. Here, the aqueous flow rate was adjusted over a range of 100 to 300  $\mu\text{L/h}$  at a constant 500  $\mu\text{L/h}$  oil flow rate. In **Fig. 6(B)**, a greater droplet size is observed as the water flow rate is increased. The generation frequency also increases as the aqueous flow rate becomes higher, as illustrated in **Fig. 6(E)**. Thus, the aqueous flow has an opposite effect on the droplet size as compared to the oil flow. However,

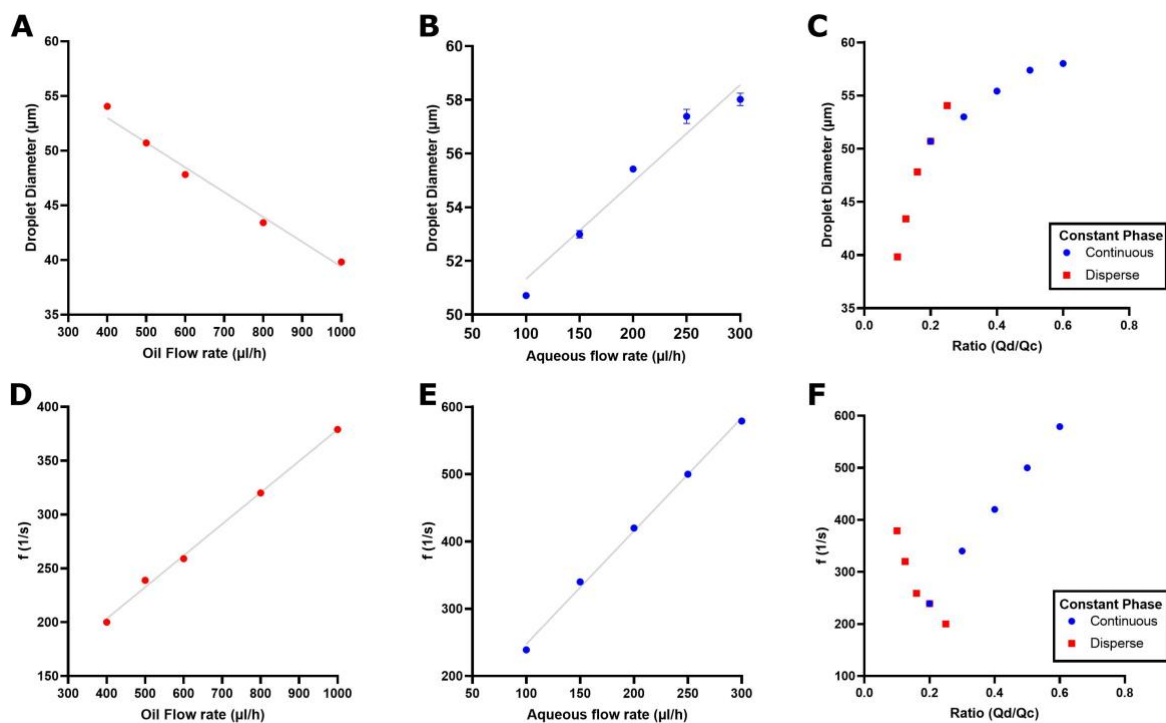


**Fig. 6 – Numerical investigations of the effect of the inflow conditions on both the droplet diameter and droplet generation frequency  $f$  in a 50  $\mu\text{m}$  circuit. (A,D) Constant aqueous flow rate of 100  $\mu\text{L/h}$ . (B,E) Constant oil flow rate of 500  $\mu\text{L/h}$ . (C,F) Summation of the previous graphs over the ratio of Qd to Qc.**

both flows will increase the generation frequency as their flow rate becomes greater.

These observations can be better understood when we examine the ratio between the dispersed and continuous flow rate. The droplet size decreases as the flow rate difference between both phases increases. In **Fig. 6(C)**, the difference between Qd to Qc becomes lesser as the oil flow rate decreases. This results in greater droplet diameters. Inversely, the ratio Qd/Qc lowers as the water flow rate increases in **Fig. 6(C)**. Thus, the droplet diameter increases when the aqueous flow is increased.

The generation frequency will increase as the total volume flow rate increases. At a constant dispersed flow rate in **Fig. 6(F)**, the highest frequency is seen at a higher ratio since the greatest total volume flow rate is found at this point. At a constant continuous flow rate, a higher generation frequency is observed as the aqueous flow rate increases, even though the ratio becomes lower as demonstrated in **Fig. 6(F)**.

A similar numerical and experimental investigation on droplet-based microfluidic devices by Soroor *et al.* demonstrated the same trends for the resulting droplet sizes and generation frequencies (25). At a constant dispersed phase flow rate, the droplet size increased as the ratio of Qd to Qc became smaller by decreasing the oil flow rate. They also showed a higher generation frequency at a higher ratio where the continuous

flow rate is greater when the dispersed flow rate is constant. Although, a similar flow-focusing junction was utilized, the exact values are not comparable since the channel dimensions and the fluid flow rates differ between both studies.

*Experimental Investigation* – After the characterization process, the most qualified devices, which showed the least amount of contamination, were selected for the experimental investigation. The functionality of the filter module in the inlets of the devices is demonstrated in **Supplementary Fig. 3**. A microfluidic device with 50- $\mu\text{m}$ -wide channels was inserted into the experimental setup to evaluate both the droplet size and generation frequency for different flow conditions. First, the oil pressure was increased from 150 to 500 mbar, while the aqueous pressure was kept at a constant pressure of 75 mbar, as shown in **Fig. 7(A)**. Additionally, a new microfluidic circuit with similar properties was utilized to evaluate the reproducibility of the measurements (**Supplementary Fig. 4**). In both cases, the droplet diameter decreased as a higher oil pressure was applied. Moreover, in **Fig. 7(C)**, a higher droplet generation frequency is demonstrated over an increasing oil pressure since this results in a larger difference between Qd and Qc. The same trend was not observed in **Supplementary Fig. 4**. This illustrates the inconsistencies between different measurements,

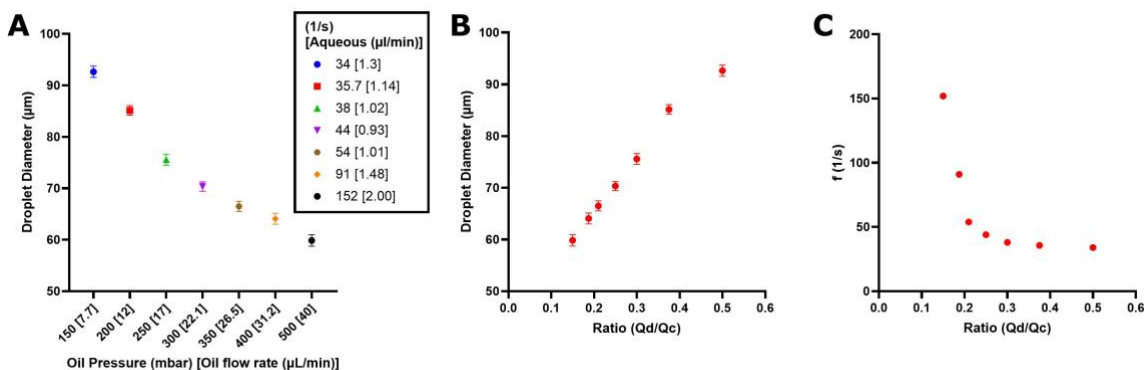


**Fig. 7 – Experimental investigation of a changing oil pressure at a fixed aqueous pressure of 75 mbar in a 50- $\mu\text{m}$ -wide channel.** (A) The resulting droplet diameter as the oil pressure is increased. The flow rates were measured by the flow sensor in the setup. The generation frequency is also given for each point (B) The influence of the ratio Qd/Qc on the droplet diameter. (C) The effect of the ratio Qd/Qc on the generation frequency.

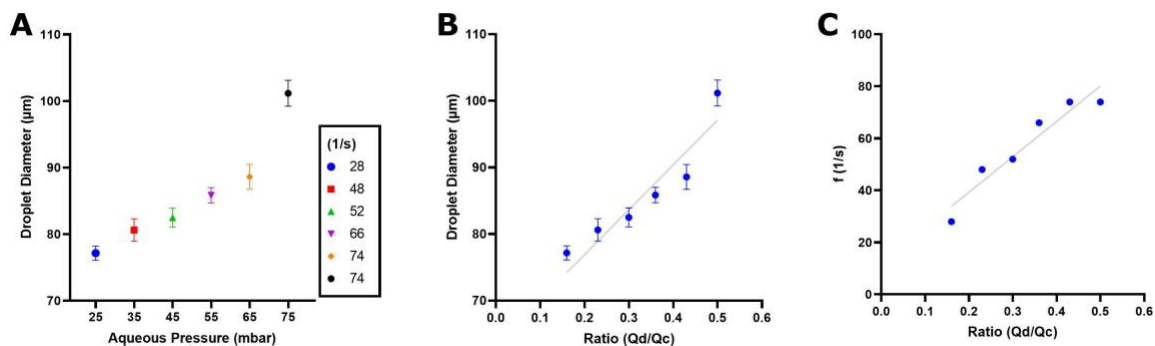


**Fig. 8 – Experimental investigation of a changing aqueous pressure at a fixed continuous pressure of 150 mbar in a 50-µm-wide channel.** (A) The resulting droplet diameter as the water pressure is increased. The generation frequency  $f$  is also given for each point (B) The influence of the ratio  $Q_d/Q_c$  on the droplet diameter. (C) The effect of the ratio  $Q_d/Q_c$  on the generation frequency.

which could be caused by instable flow rates or contaminations in the circuit.

Secondly, the effect of an increasing aqueous pressure at a constant oil pressure was investigated. The water pressure was increased from 25 to 75 mbar, while the oil pressure was 150 mbar. This experiment was also performed two times in two different devices with 50-µm-wide channels (Fig. 8 and Supplementary Fig. 5). In Fig. 8(A, B), a greater droplet size is seen as the aqueous flow becomes higher. The generation frequency also steadily increases over the experiment as shown in Fig. 8(C). In Supplementary Fig. 5, the droplet size increases in a similar range, but some deviating measurements were observed. These inconsistencies were also measured by the flow sensors during the experiment. The obtained flow rates of both fluids demonstrate the instability of the measurements, which could explain the deviating data.

This initial experiment illustrated some difficulties for *in vitro* testing of the devices. It was not possible to control the fluid flows by setting a constant flow rate condition for both fluids since this results in an unstable system. The flows are constantly interacting with each other in the device and the difference between the flow conditions of both phases is relatively high. Thus, the system remains unstable as the flow sensors are caught in a feedback loop. Even when operating the pump in a pressure-driven mode, it is still important to allow the system to stabilize between each measurement. The presence of air bubbles or any contamination in the microfluidic channels often interrupted the fluid

flow. This resulted in either unstable flows or no flow at all.

Next, a microfluidic device with 30-µm-wide channels was utilized to study the effect of the channel geometry on the droplet size and generation frequency. In Fig. 9(A, B), the pressure of the dispersed phase was increased from 100 to 500 mbar at a constant continuous phase pressure of 800 mbar. The droplets became bigger as the water pressure was increased and the ratio of  $Q_d$  to  $Q_c$  lowered. More droplets were generated as the pressure of the aqueous phase became higher as shown in Fig. 9(C). A similar experiment in which the oil pressure is increased at a constant dispersed phase pressure of 300 mbar is illustrated in Fig. 9(D, E, F). The resulting droplet generation frequency did increase as a greater flow of the continuous phase was achieved. Additionally, smaller droplets were observed at higher oil pressures.

The effect of different channel geometries was more difficult to illustrate in the experimental data as the pumps were operated in pressure-driven mode. This way, it is not possible to directly compare the 50-µm-wide circuits to the 30-µm-wide channels since the resistances found in both channels are inherently different. A higher pressure would be necessary in a narrow channel to obtain a similar flow rate as a broader channel. Therefore, the pressure values cannot be compared directly. The effect of the channel geometry becomes apparent when comparing the results of a 50-µm-wide (Fig. 7) and a 30-µm-wide channel (Supplementary Fig. 6(D, E, F)) with similar flow

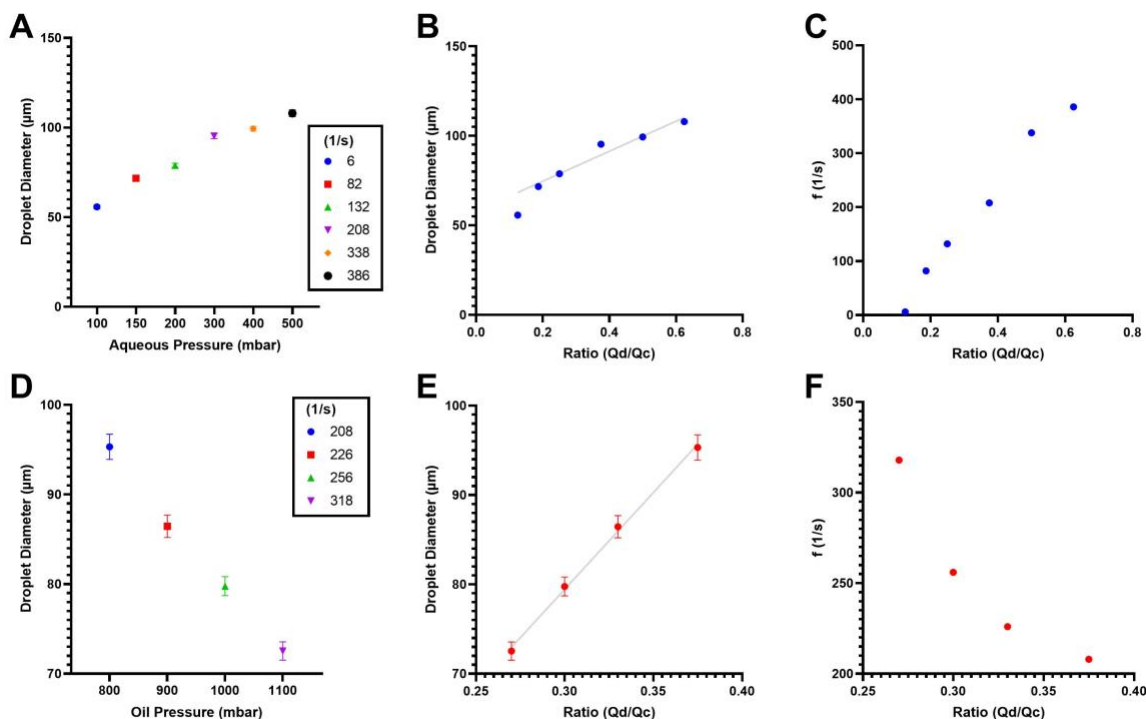


**Fig. 9 – Experimental investigation of the droplet tunability in a 30-µm-wide circuit. (A,B,C)** Constant oil pressure of 800 mbar. **(D, E, F)** Constant aqueous pressure of 300 mbar. **(A)**The resulting droplet diameter as the water pressure is increased. The generation frequency  $f$  is also given for each point **(B)** The influence of the ratio Qd/Qc on the droplet diameter. **(C)** The effect of the ratio Qd/Qc on the generation frequency. **(D, E, F)** The effect of an increasing oil pressure on the droplet diameter and generation frequency.

rates. However, this comparison is quite rough due to the instabilities in the measured flow rates. Here, the oil flow rate is increased from 12 to 30 µL/min at an approximately constant aqueous flow rate of 1 µL/min. In the 50-µm-wide circuit, the droplet diameter is decreased from 85.1 to 64.1 µm. In a 30-µm-wide circuit, the droplet diameter decreases from 81.7 to 60.4 µm. Thus, the resulting droplets of the smaller channel are slightly smaller than the ones resulting from a broader channel at similar flow rates for both fluids. At a narrow nozzle, a narrow stream is established within the flow focusing junction. However, in the larger nozzle the size of the water stream is larger in size since a greater amount of water is injected from the stream into the resulting droplet at any given moment (26). This may explain the slightly bigger droplets observed at a broader channel.

The effect of the channel geometry should be further investigated after the development of a more stable flow. Firstly, the presence of air bubbles or

any contaminations in the circuit should be reduced in order to create a generally more stable flow. The circuit can be flushed with ethanol 99% to remove any unwanted particles (25). Secondly, the fluid flows should be fully developed before the start of any measurements. This can be done by waiting several minutes before recording the actual data.

During this *in vitro* investigation, we had to manually analyze the resulting data. However, this could be improved by creating an automatic alternative for this process. Here, a software such as droplet morphometry and velocimetry (DMV) could significantly speed up this process, which allows for more data and more accurate results (27). Similar results could be achieved by using the automated droplet measurement (ADM) software (28). Both programs potentially allow for the rapid tracking of droplets. They can also provide additional information such as neighbor spacing, shape deformation, and pixel statistics.

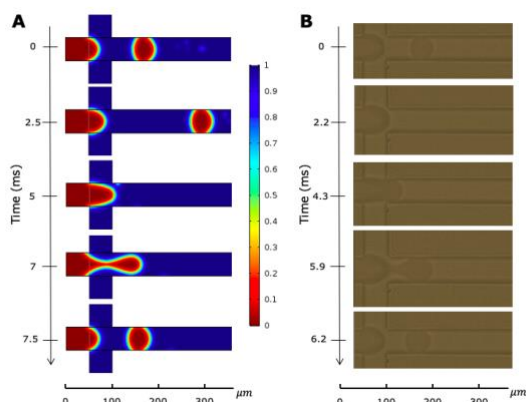


**Fig. 10 – Numerical and experimental investigation of the droplet generation at a similar flow-focusing junction.** (A) The simulated droplet generation is achieved by applying a 50  $\mu\text{L}/\text{h}$  and 400  $\mu\text{L}/\text{h}$  flow rate to the dispersed and continuous phase, respectively. (B) The experimental droplet generation is achieved by applying a pressure of 50 mbar and 400 mbar to the dispersed and continuous phase, respectively.

*Comparison in silico and in vitro* – The obtained numerical and experimental results demonstrate similar trends. At a constant dispersed inflow condition, the droplet size increases and the droplet generation frequency decreases as the ratio of Qd to Qc becomes lower since the continuous flow decreases in this manner. This trend is observed in both numerical (Fig. 3 and 6) and experimental (Fig. 7 and 9) data. Similarly, at a constant continuous inflow condition, the droplet size increases and the droplet generation frequency increases as the ratio of Qd to Qc becomes lesser since the dispersed flow increases in this way. This trend is also observed in both numerical (Fig. 3 and 6) and experimental (Fig. 8 and 9) data. As noted, these trends were also observed in both numerical and experimental results by Soroor *et al.*(25). Furthermore, a similar study was performed by Sartipzadeh *et al.* in which the effect of the channel geometry was thoroughly investigated (29). This work also shows the correlations between the ratio of Qd to Qc and the resulting droplet sizes at fixed dispersed phase flow rates. Similarly, the correlation between the generation frequency and the ratio of Qd/Qc is studied. In both cases, the same trends are seen as the ones found in this work. At a fixed dispersed flow rate, the droplet generation frequency decreases as the difference

between Qd and Qc becomes smaller. Inversely, the droplet size increases as the ratio Qd/Qc lowers.

A visual comparison between the numerical and experimental results with a similar Qd/Qc ratio of 0.125 can be seen in Fig. 10. In Fig. 10(A), the droplet formation at the flow-focusing junction *in silico* is demonstrated. Here, the flow rates of the aqueous and continuous phase are 50  $\mu\text{L}/\text{h}$  and 400  $\mu\text{L}/\text{h}$ , respectively. In Fig. 10(B), an experimental measurement of the droplet formation with a aqueous pressure of 50 mbar and an oil pressure of 400 mbar is demonstrated. Both experiments are performed using a 50  $\mu\text{m}$ -wide-channel and the inflow condition ratio is in both cases 0.125. Moreover, this specific experimental measurement was performed using only HFE-7500 oil in absence of dSurf as the continuous phase, which was the case in all the previous measurements. Thus, the dynamic viscosity and the density properties of the fluids were exactly the same in both the numerical and experimental results in Fig. 10. Only the inflow boundary condition was defined as a flow rate *in silico* and as a pressure *in vitro*. The resulting droplet size of the simulated data is 50.7  $\mu\text{m}$  at a frequency of 133 droplets per second. The experimental data showed a generation frequency of 161 droplets per second with an average droplet size of 58.1  $\mu\text{m}$ . This illustrates the great resemblance between the *in silico* visualization and *in vitro* results in Fig. 10. However, there are obvious differences between both measurements since the flow rates of the fluids were not exactly matched between both the simulated and the experimental data.

## CONCLUSION

This work serves as a foundation for the development of a droplet-based microfluidic device for the charge-mediated assembly of dsGUVs. This enables a high-throughput generation of monodisperse droplets, together with considerable control over the particle size, and great stability. In the present study, the full development process of a microfluidic device was demonstrated to improve future devices. The in-house fabrication of the masters and replicas was optimized by prolonging the soft bake time of SU-8 photoresist to 30 minutes and the utilization of a spacer. It was also beneficial to use the SU-8 photoresist 3025 dilution with a lower viscosity to prevent air bubble formation. Moreover, it is necessary to use a layer of Omnicoat

on glass cover slides before applying the SU-8 photoresist to improve adhesion forces between both materials. Both an *in silico* and *in vitro* investigation of the microfluidic devices was performed. Generally, the ratio of Qd to Qc determines both the resulting droplet size and the droplet generation frequency. These droplet parameters were tunable in a certain range by adjusting the inflow conditions of both fluids. Furthermore, devices with narrower channels produced smaller droplets at a higher rate as compared to wider channels. Similar trends were observed between the simulations and the experimental measurements, which is beneficial for future projects.

These results show the possible tunability of the water-in-oil droplet parameters when utilizing this microfluidic chip. The addition of a collection chamber, which has a height of 100  $\mu\text{m}$ , at the end of the microfluidic device would offer a better insight in the exact sizes of the resulting droplets. Currently, all droplets with a diameter greater than 50  $\mu\text{m}$  seem even bigger since they are flattened between both surfaces of the microfluidic device. The formation of dsGUVs can start, once spherical water-in-oil droplet, which are smaller than the channel dimensions, are observed. This can be potentially achieved by further increasing the continuous phase flow rate at a constant aqueous phase flow rate. In the following stages of this project, these droplets will function as scaffolding for the charge-mediated assembly of dsGUVs. First, SUVs will be introduced into the aqueous inlet with a 2 mM final lipid concentration, and 30 mM Tris buffer and 10 mM  $\text{Mg}^{2+}$  ion concentrations. The continuous phase will consist of HFE-7500 oil, which includes 1.4 wt% PFPE-PEG-based fluorosurfactants and 9 mM Krytox. Now, water-in-oil droplets, which contain the SUV solution, will be formed at the flow-focusing junction. The negatively-charged surfactant Krytox will mix with the PEG-based fluorosurfactants, and

assemble at the droplet periphery. The negatively charged inner droplet interface attracts the  $\text{Mg}^{2+}$  ions, which promotes SUV adhesion and rupture at this location. In this manner, a lipid bilayer will form at the droplet periphery and cover the entire co-polymer stabilized water-in-oil droplet. This results in the formation of dsGUVs or artificial membranes (23).

An alternative microfluidic approach illustrates a pH-mediated assembly of dsGUVs, making the presence of charged species redundant (30). This alternative approach can be useful when the cargo, which will be encapsulated in the GUVs, is sensitive to charged species.

Further steps in this process include the manipulation of dsGUVs with pico-injection technology. This technique would allow to sequentially load the artificial membranes with precise amounts of active compounds or membrane proteins at high-throughput rates. This process is easier in droplet-stabilized GUVs since the oil and the oil additives promote a more stable environment. Moreover, the pico-injection technology can be incorporated into the microfluidic device to perform all necessary steps in one process (8, 13). As noted, the utilization of these artificial membranes to reconstitute GPCRs could potentially lead to significant advances in the drug screening process for GPCRs. The artificial membranes can function as simplified versions of eukaryotic cells, while the GPCRs are more stabilized in a membrane than their purified counterparts (6). Lastly, the functionalized dsGUVs can be released into a physiological environment to form functionalized GUVs, which in turn can be useful for further investigations such as drug screening or membrane-bound process investigations. Thus, the obtained results will pave the way for the further development of droplet-based microfluidic devices, which can be utilized in bottom-up synthetic biology applications and beyond.

*Acknowledgements* – S.B. is grateful for the support and advice provided by the personal of both the research group of Biomedical Device Engineering and the research group of Dynamic Bioimaging Lab. S.B. gives a special thanks to Stijn Dilissen, Prof. dr. Jelle Hendrix and Prof. dr. ir. Ronald Thoelen for their guidance and support during this research.

*Author contributions* – S.B. performed the numerical investigations, the fabrication of the microfluidic devices, the characterization of the devices, the experimental investigations, and the data analysis. S.D. helped with the optimization of the fabrication process, the characterization of the devices, and the experimental investigations. Investigation, S.B., S.D.; writing, S.B.; supervision - review, S.D., R.T.; guidance, S.D., R.T., J.H.

## REFERENCES

1. Stauer O, Antona S, Zhang D, Csatári J, Schröter M, Janiesch J-W, et al. Microfluidic production and characterization of biofunctionalized giant unilamellar vesicles for targeted intracellular cargo delivery. *Biomaterials*. 2021;264:120203.
2. Stauer O, Dietrich F, Rimal R, Schröter M, Fabritz S, Boehm H, et al. Bottom-up assembly of biomedical relevant fully synthetic extracellular vesicles. *Sci Adv*. 2021;7(36):eabg6666-eabg.
3. Lussier F, Stauer O, Platzman I, Spatz JP. Can Bottom-Up Synthetic Biology Generate Advanced Drug-Delivery Systems? *Trends in Biotechnology*. 2021;39(5):445-59.
4. Zhang Y, Ruder WC, LeDuc PR. Artificial cells: building bioinspired systems using small-scale biology. *Trends Biotechnol*. 2008;26(1):14-20.
5. Elani Y. Construction of membrane-bound artificial cells using microfluidics: a new frontier in bottom-up synthetic biology. *Biochem Soc Trans*. 2016;44(3):723-30.
6. Yasi EA, Kruyer NS, Peralta-Yahya P. Advances in G protein-coupled receptor high-throughput screening. *Current Opinion in Biotechnology*. 2020;64:210-7.
7. Heng BC, Aubel D, Fussenegger M. An overview of the diverse roles of G-protein coupled receptors (GPCRs) in the pathophysiology of various human diseases. *Biotechnology Advances*. 2013;31(8):1676-94.
8. Weiss M, Frohnmayer JP, Benk LT, Haller B, Janiesch J-W, Heitkamp T, et al. Sequential bottom-up assembly of mechanically stabilized synthetic cells by microfluidics. *Nature Materials*. 2018;17(1):89-96.
9. Biner O, Schick T, Müller Y, von Ballmoos C. Delivery of membrane proteins into small and giant unilamellar vesicles by charge-mediated fusion. *FEBS Letters*. 2016;590(14):2051-62.
10. Deng N-N, Yelleswarapu M, Huck WTS. Monodisperse Uni- and Multicompartment Liposomes. *Journal of the American Chemical Society*. 2016;138(24):7584-91.
11. Wang L, Tonggu L. Membrane protein reconstitution for functional and structural studies. *Science China Life Sciences*. 2015;58(1):66-74.
12. Göpfrich K, Haller B, Stauer O, Dreher Y, Mersdorf U, Platzman I, et al. One-Pot Assembly of Complex Giant Unilamellar Vesicle-Based Synthetic Cells. *ACS synthetic biology*. 2019;8(5):937-47.
13. Göpfrich K, Platzman I, Spatz JP. Mastering Complexity: Towards Bottom-up Construction of Multifunctional Eukaryotic Synthetic Cells. *Trends in Biotechnology*. 2018;36(9):938-51.
14. Angelova MI, Dimitrov DS. Liposome electroformation. *Faraday Discussions of the Chemical Society*. 1986;81(0):303-11.
15. Reeves JP, Dowben RM. Formation and properties of thin-walled phospholipid vesicles. *Journal of Cellular Physiology*. 1969;73(1):49-60.
16. Moscho A, Orwar O, Chiu DT, Modi BP, Zare RN. Rapid preparation of giant unilamellar vesicles. *Proceedings of the National Academy of Sciences*. 1996;93(21):11443.
17. Seantier B, Kasemo B. Influence of Mono- And Divalent Ions on the Formation of Supported Phospholipid Bilayers via Vesicle Adsorption. *Langmuir*. 2009;25(10):5767-72.
18. Shigematsu T, Koshiyama K, Wada S. Effects of Stretching Speed on Mechanical Rupture of Phospholipid/Cholesterol Bilayers: Molecular Dynamics Simulation. *Scientific Reports*. 2015;5(1):15369.
19. Hardy GJ, Nayak R, Zauscher S. Model cell membranes: Techniques to form complex biomimetic supported lipid bilayers via vesicle fusion. *Current Opinion in Colloid & Interface Science*. 2013;18(5):448-58.

20. Martino C, deMello AJ. Droplet-based microfluidics for artificial cell generation: a brief review. *Interface Focus*. 2016;6(4):20160011.
21. Deshpande S, Caspi Y, Meijering AEC, Dekker C. Octanol-assisted liposome assembly on chip. *Nature communications*. 2016;7:10447-.
22. Hu PC, Li S, Malmstadt N. Microfluidic Fabrication of Asymmetric Giant Lipid Vesicles. *ACS Applied Materials & Interfaces*. 2011;3(5):1434-40.
23. Haller B, Göpflich K, Schröter M, Janiesch J-W, Platzman I, Spatz JP. Charge-controlled microfluidic formation of lipid-based single- and multicompartments systems. *Lab on a Chip*. 2018;18(17):2665-74.
24. Janiesch J-W, Weiss M, Kannenberg G, Hannabuss J, Surrey T, Platzman I, et al. Key Factors for Stable Retention of Fluorophores and Labeled Biomolecules in Droplet-Based Microfluidics. *Analytical Chemistry*. 2015;87(4):2063-7.
25. Soroor M, Zabetian Targhi M, Tabatabaei SA. Numerical and experimental investigation of a flow focusing droplet-based microfluidic device. *European Journal of Mechanics - B/Fluids*. 2021;89:289-300.
26. Rahimi M, Shams Khorrami A, Rezai P. Effect of device geometry on droplet size in co-axial flow-focusing microfluidic droplet generation devices. *Colloids and Surfaces A: Physicochemical and Engineering Aspects*. 2019;570:510-7.
27. Basu AS. Droplet morphometry and velocimetry (DMV): a video processing software for time-resolved, label-free tracking of droplet parameters. *Lab on a Chip*. 2013;13(10):1892-901.
28. Chong ZZ, Tor SB, Gañán-Calvo AM, Chong ZJ, Loh NH, Nguyen N-T, et al. Automated droplet measurement (ADM): an enhanced video processing software for rapid droplet measurements. *Microfluidics and Nanofluidics*. 2016;20(4):66.
29. Sartipzadeh O, Naghib SM, Seyfoori A, Rahmanian M, Fatemina FS. Controllable size and form of droplets in microfluidic-assisted devices: Effects of channel geometry and fluid velocity on droplet size. *Materials Science and Engineering: C*. 2020;109:110606.
30. Lussier F, Schröter M, Diercks NJ, Jahnke K, Weber C, Frey C, et al. pH-Triggered Assembly of Endomembrane Multicompartments in Synthetic Cells. *ACS Synthetic Biology*. 2022;11(1):366-82.

Supplementary Information

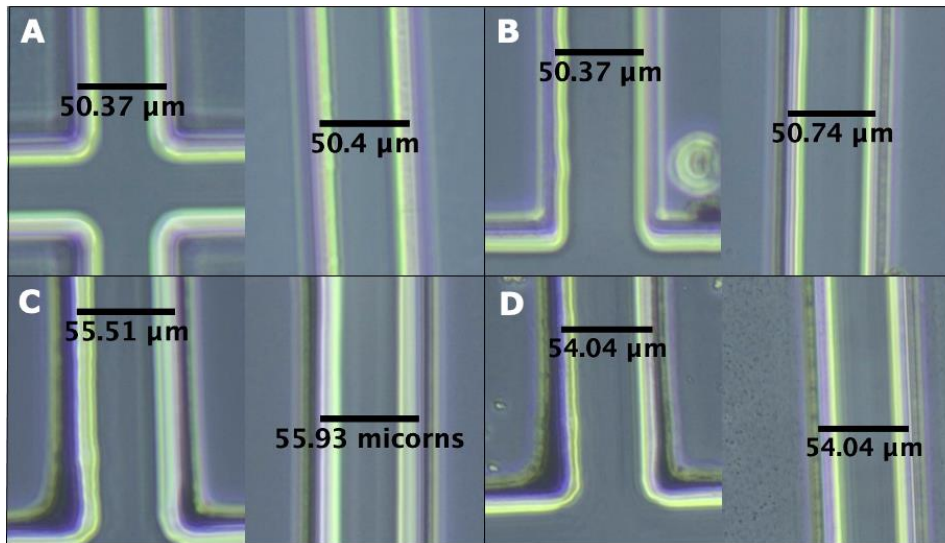


**Fig. S1: effect spacer (A,B)** Photo lithography without the use of a spacer. **(C, D)** Photo lithography with the use of a spacer, which has a height of 50 μm.

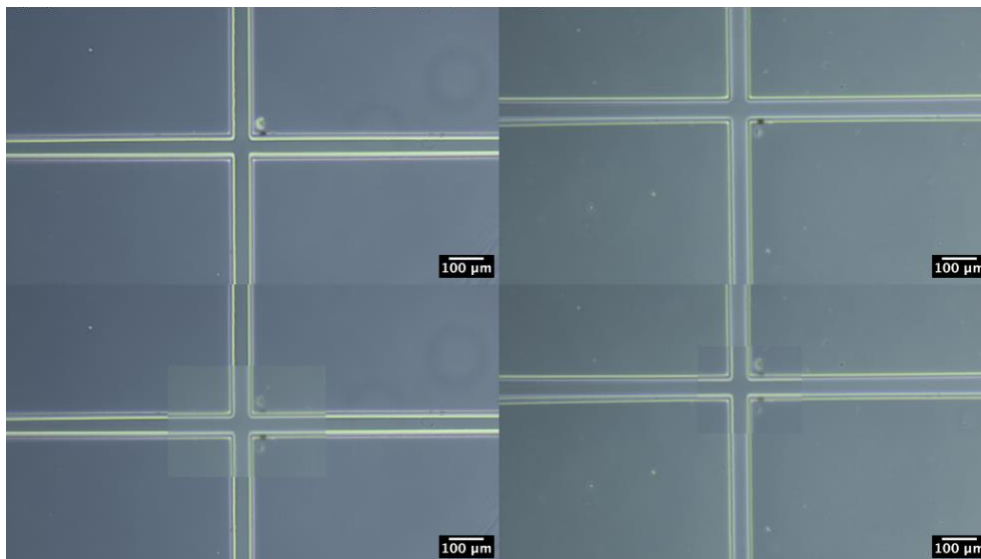


**Fig. S2: The difference between the SU-8 photoresist master and the PDMS-based replica. (A)** Master **(B)** Replica **(C)** The replica is overlapped by the master. **(D)** The master is overlapped by the replica.

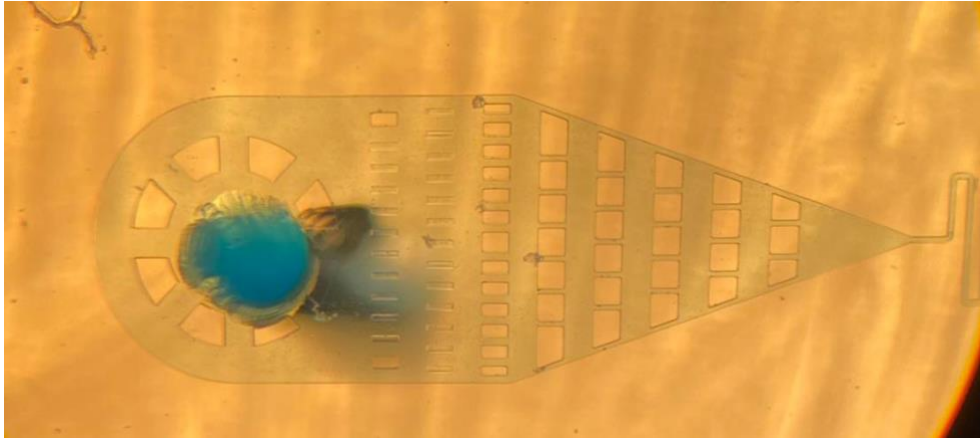


Fig. S3: Filtering module at the inlet.

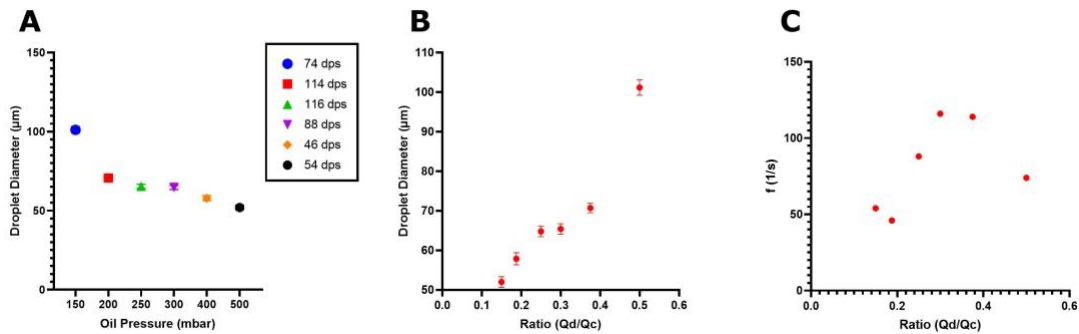


Fig. S4: Experimental investigation in a 50- $\mu\text{m}$ -wide channel. Constant water pressure of 75 mbar. The channel height is 50  $\mu\text{m}$ .

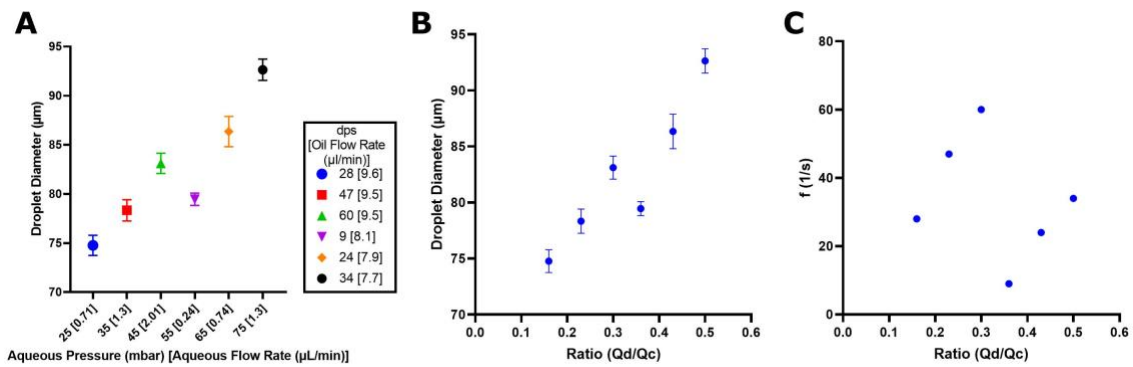
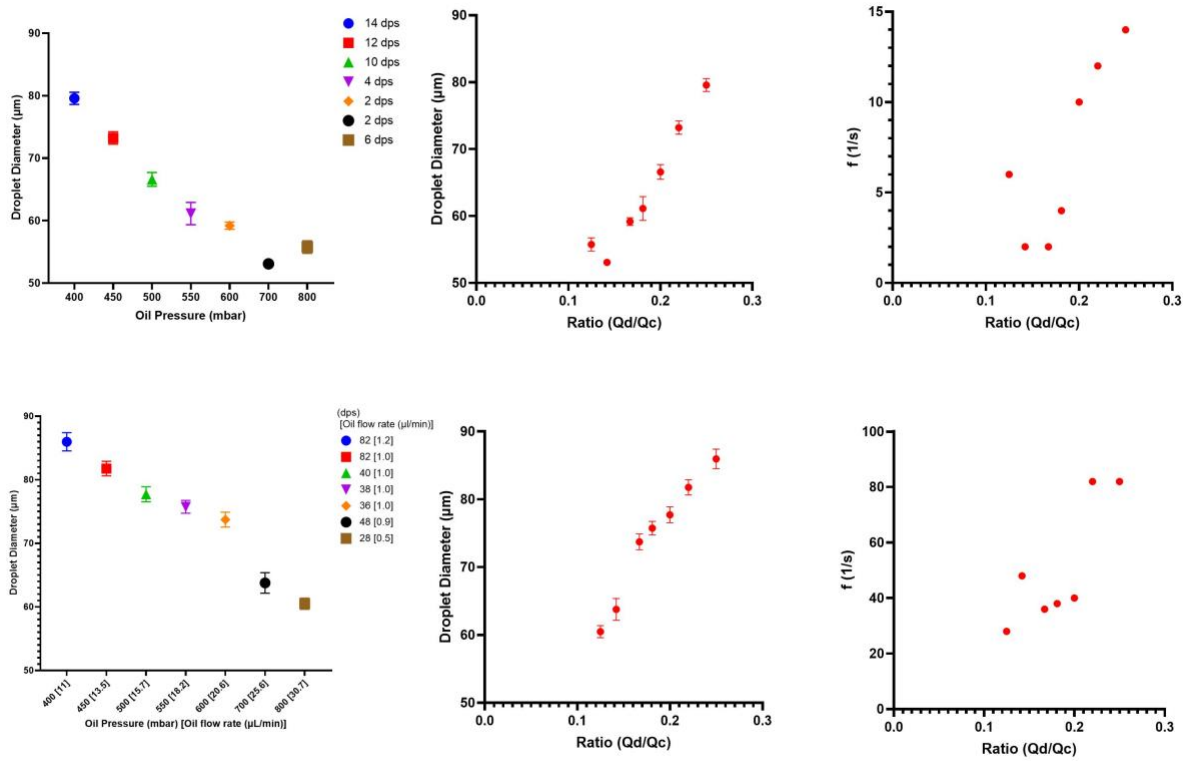


Fig. S5: Experimental investigation in a 50- $\mu\text{m}$ -wide channel. Constant oil pressure of 150 mbar. The channel height is 50  $\mu\text{m}$ .



**Fig. S6: Experimental investigation in a device with 30- $\mu\text{m}$ -wide channels.** Constant dispersed phase pressure of 100 mbar. (A, B, C) The first device and measurement without flow sensor. (D, E, F) The second device and measurement with flow sensor.